Accepted Manuscript

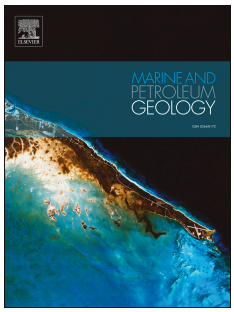

Distribution and growth styles of isolated carbonate platforms as a function of fault propagation

R. Loza Espejel, Tiago M. Alves, Tom G. Blenkinsop

PII: S0264-8172(19)30225-9

DOI: https://doi.org/10.1016/j.marpetgeo.2019.05.020

Reference: JMPG 3840

To appear in: *Marine and Petroleum Geology*

Received Date: 30 November 2018

Revised Date: 9 May 2019

Accepted Date: 15 May 2019

Please cite this article as: Loza Espejel, R., Alves, T.M., Blenkinsop, T.G., Distribution and growth styles of isolated carbonate platforms as a function of fault propagation, *Marine and Petroleum Geology* (2019), doi: https://doi.org/10.1016/j.marpetgeo.2019.05.020.

Distribution and growth styles of isolated carbonate platforms as a function of fault propagation

R. Loza Espejel, Tiago M. Alves, and Tom G. Blenkinsop

3D Seismic Lab, School of Earth and Ocean Sciences, Cardiff University, Main Building-Park Place, CF10 3AT Cardiff, United Kingdom

Abstract

Fault control on the position and distribution of isolated carbonate platforms is investigated in Northwest Australia using high quality 3D seismic and borehole data from the Bonaparte Basin. Specifically, we address the relationship between carbonate productivity and fault growth so as to understand what the primary controls on the growth of isolated carbonate platforms are. Throw-depth (T-Z) and throw-distance (T-D) profiles for normal faults suggest they formed fault segments that were linked at different times in the study area. This caused differential vertical movements: some of the normal faults have propagated to the surface, while others have upper tips 19 to 530 ms two-way-time below the sea floor, with the largest values comprising faults underneath isolated carbonate platforms. As a result, four distinct zones correlate with variable geometries and sizes of carbonate platforms, which are a function of topographic relief generated by underlying propagating faults. Some relay ramps form a preferred location for the initiation and development of carbonate platforms, together with adjacent structural highs. Due to the complex effect of fault propagation to the palaeosurface, and soft-linkage through relay ramps, three distinct models are proposed. Two models explain carbonate platform growth and one explains changes in its internal structure: (1) in the first model, fault throw is larger than carbonate productivity; (2) the second model considers fault throw to be equal or less than carbonate productivity; and (3) the third model,

fault throw post-dates the growth of the carbonate platform(s). The analysis of fault propagation vs. carbonate platform growth shown here is important, as the three models proposed potentially correlate with variable fracture densities and distributions within the carbonate platforms. Based on our results, models 2 and 3 above enhance fracture- and fault-dominated porosity and permeability to a greater degree, making them a good target for hydrocarbon exploration.

Keywords: Isolated carbonate platforms; continental margins; Northwest Australia; fault growth; throw distribution; fractured reservoir.

1 Introduction

Isolated carbonate platforms (ICPs) are of great interest to petroleum exploration due to their reservoir potential. Some of the best examples of such potential are recorded in the South China Sea (Neuhaus et al., 2004; Ding et al., 2014; Hutchison, 2014), Kazakhstan (Collins et al., 2006; Kenter et al., 2008; Collins et al., 2016), the Middle East (Alsharhan, 1987), the Brazilian Coast (Buarque et al., 2017), the Barents Sea (Blendinger et al., 1997; Elvebakk et al., 2002; Nordaunet-Olsen, 2015; Alves, 2016), amongst others. It is estimated that reserves of about 50 billion barrels of oil equivalent are accumulated within these structures around the world (Burgess et al., 2013) including fields such as the Luconia Province and the Malampaya Field in the South China Sea (Neuhaus et al., 2004; Zampetti et al., 2004; Rankey et al., 2019), the Karachaganak gas-condensate-oil field and the Tengiz field in the Pre-Caspian Basin, Kazakhstan (Elliott et al., 1998; Collins et al., 2006; Borromeo et al., 2010; Katz et al., 2010).

Isolated carbonate platforms are carbonate deposits that accumulate *in situ* as geomorphic features with significant topographic expression relative to adjacent, time-equivalent strata (Burgess et al., 2013). These isolated carbonate platforms tend to have a flat top as a result of the constrained space for vertical carbonate accommodation limited by the sea level (Schlager, 2005). These carbonate platforms are also characterised by presenting steep margins on their edges (Schlager, 2005). As such, isolated carbonate platforms show no significant attachment to a continental landmass. They can comprise several depositional environments such as reefs, lagoons, tidal flats and flanking slopes (Stanton Jr, 1967; Burgess et al., 2013). Structural elements (such as faults), palaeotopography, environment (penetration of light to the seafloor, temperature, nutrients and salinity) and distinct biologic assemblages are some of the mechanisms that, when combined, influence the timing, location, growth and development of isolated carbonate platforms (Schlager, 2005). For instance, propagation of a fault to the surface can modify the seafloor topography, which in turn can influence carbonate platform development.

Research has been focused on the controls and genetics of isolated carbonate platforms in a large, regional basin-scale (Bosence, 2005; Dorobek, 2007). Additionally, the stratigraphic relationships and depositional contact with structural features have been generalised (Dorobek, 2007). Detailed structural controls have been previously studied focusing primarily on structural highs of sedimentary basins (Zampetti et al., 2004; Saqab and Bourget, 2015a). In contrast to the published literature, this paper focuses on the Karmt Shoals area to understand how underlying propagating faults can control carbonate growth and the morphology of ICPs in the Bonaparte Basin (Fig. 1). Saqab and Bourget (2015a) have already undertaken an analysis of fault controls on ICPs in this area with a focus on the "Big Bank" platform located to the northeast of the Karmt Shoals, using a different seismic and well dataset. However, quantitative measurements have not been completed in depth, below

the ICPs imaged on the present-day sea floor. Understanding the relationship between carbonate productivity and fault history can provide useful information in regions with complex extensional faults in synrift settings such as the North West Shelf of Australia; where footwall areas and structural highs (horsts) interact with the carbonate accumulation, isolating the clastic supply (Bosence, 2005). Fault growth history can also be used to provide important insights into the development and timing of ICPs, as well as their relationship with carbonate productivity rates.

The Bonaparte Basin (Fig. 1) presents Neogene deposits that are mainly composed of carbonate successions over which isolated carbonate platforms have developed since the Pleistocene (Saqab and Bourget, 2015a). Isolated carbonate platforms started to develop in areas recording changes in topography in the early stages of the Quaternary (Mory, 1991; Saqab and Bourget, 2015a). Some of these platforms were controlled by structural highs (horsts) in a highly faulted region (Burgess et al., 2013). However, the platforms in the study area have a much more complex story with different periods of faulting and fault reactivation. Therefore, a simple description relating their initiation to a unique mechanism cannot completely address the geological and oceanographic settings in which they were formed. The observed spatial distribution of ICPs relative to fault position suggests more complex controls than just the faulting. There is a good number of isolated carbonate platforms that are not positioned on structural highs and their interior is cross-cut by faults. In detail, this work intends to address the following questions:

a) How does the surface fault propagation influence the growth styles and distribution of ICPs, and what is the relationship between carbonate accumulation and fault throw?
b) How can we facilitate the prospect identification of ICPs and predict the best structural setting for hydrocarbon accumulation?

2 Data and methods

The seismic data used in this study includes a 3D seismic volume (Karmt3D AGC Time) located in the northern part of the Vulcan Sub-Basin, Timor Sea (Fig. 1). The seismic volume was acquired by Geco-Prackla in 1996 for Woodside Offshore Petroleum, covering more than 2,000 km^2 with a 6 s vertical penetration (Carenzi and Cazzola, 2008). The volume was provided by Geoscience Australia and comprises 3334 inlines (IL) and 5191 crosslines (XL) with a 12.35 x 12.50 m line spacing and a vertical sampling interval of 4 ms. The frequency spectra of the interpreted volume in the first 3,000ms ranges from 10 to 70 Hz, with an average value of around 20 Hz.

The seismic data is in time domain and of very good quality in the Cenozoic interval, allowing for a very detailed analysis of structures and ICPs (Figs. 2 and 3). The survey has been processed by Veritas DGC in 1997 to correct pull-up effects and poor reflector continuity beneath the ICPs (Ruig, 2000; Carenzi and Cazzola, 2008). These pull-up effects are related to differences in lithology. In general, the carbonates within the ICPs have a higher (V_p) velocity than the surrounding strata. Moreover, the ICPs have a steep angle of slope, which made the data acquisition and processing more complex due to the angle that the acoustic waves were penetrating the subsurface in those areas (Fig. 4). As a result, the pull-up effects increase underneath these regions, as well as the stretched rims of the platforms (Figs. 3 and 4). Despite the efforts to correct pull-up effects, residual effects are still present on the seismic volume (Fig. 4). In variance time slices below the ICPs, as a result of pronounced velocity pull-up effects, the platform outlines are still observed (Fig. 4). In profile view, these effects could be mistakenly interpreted as faults with sub-circular horst-like structures, but normally the strata is continuous across the pull-up zones (Marfurt and Alves, 2015) (Fig. 4).

Well completion data and proprietary geological reports from four different wells (Mandorah-1, Ludmilla-1, Lameroo-1 and Fannie Bay-1) were used in seismic-well

123 correlations (Fig. 5). Seismic well-tie was performed using check-shots and time-depth
124 (TWT-Z) tables found in the well reports. Well completion data include stratigraphic and
125 lithological descriptions based on cuttings and sidewall core samples (Woodall, 1990;
126 Rexilius et al., 1998a; Willis, 1998; Willis, 1999b; Willis, 1999c; Willis, 1999a; Willis,
127 2000). Wireline logs (gamma ray, resistivity, density, sonic) were digitised from raster
128 composite well logs to be used for correlation of stratigraphic surfaces and depositional units
129 (Figs. 5 and 6). Micropaleontological analyses of benthonic and planktonic foraminifera, as
130 well as calcareous nannoplankton of three wells (Mandorah-1, Ludmilla-1 and Fannie Bay-
131 1), allowed the correlation of wells and the age control estimation (Rexilius et al., 1998b;
132 Rexilius et al., 1998a; Rexilius and Powell, 1999b; Rexilius and Powell, 1999a) (Fig. 5).
133 Modern bathymetric data (taken from Geoscience Australia, Fig. 1) contributed to determine
134 the depth, size, shape and position of the ICPs at present.

135

136 ***2.1 Seismic interpretation***

137 Horizon and fault interpretation were performed in both vertical and map sections using
138 seismic amplitude and coherence data (Fig. 4). Key seismic reflectors were mapped in the 3D
139 volume following basic stratigraphic principles (Alves et al., 2006; Catuneanu, 2006; Mattos
140 et al., 2016) so as to identify the primary stratigraphic events from the Base Paleocene (H_1) to
141 the modern sea floor (SF) (Figs. 2 and 7). Well-log (gamma ray, resistivity, bulk density,
142 neutron porosity and sonic) and biostratigraphic data from four exploratory wells were
143 integrated into the seismic volume (Fig. 6). The seismic surfaces and units were also
144 compared with previous interpretations by Willis (1998) (Figs. 5, 6, 7 and Table 1).

145 Key seismic horizons were mapped every 150 m in NE-SW and NW-SE amplitude
146 seismic sections using strictly seeded autotracking parameters on Schlumberger Petrel®.

Isochron maps were calculated based on the interpreted horizons in order to determine the variation in thickness of the different units (Fig. 8). For the fault interpretation, a variance attribute was extracted to better define major seismic discontinuities (e.g. fault, channels, karst features) (Figs. 4 and 9). Variance compares the similarity of traces in all directions on an interpreted surface (Chopra and Marfurt, 2007), highlighting prominent discontinuities such as faults and fractures (Brown, 2011; Marfurt and Alves, 2015). Faults were initially mapped on variance time slices to determine their length and strikes. The strikes of the faults do not coincide with the inlines (IL) or crosslines (XL) of the seismic survey (Figs. 9 and 10). These sections cross-cut the fault with an arbitrary angle (β) between the IL or XL and the strike of the fault. Therefore the interpreted faults in these sections show the apparent dip (α_2) of the fault, which is less than the real dip (α_1) (Fig. 10) and can lead to erroneous data when throw measurements are performed. For this reason, perpendicular sections to the strike of the fault at each point of interest (Fig. 10a) were created. These sections are key to visualise the real (maximum) dip (α_1) of the fault (Fig. 10b) and facilitate the interpretation, which in turn provide the maximum throw values that are required to obtain good quality data for the T-Z and T-D plots. This method is key for the fault throw analysis to avoid inaccurate data leading to erratic results. Fault linkage structures such as relay ramps are present in the study area, and their recognition was deemed important to understand the way(s) fault segments are linked in the study area. Different zones were established based on features observed on a coherence map in order to facilitate the description of the different fault sets and types of ICPs (Figs. 9b, 11, 12 and 13).

2.2 Fault throw

Fault throw measurements were taken from different fault segments to create detailed fault throw-depth (T-Z) (Fig. 14) and throw–distance (T-D) profiles (Fig. 15c) and thus generate a high-resolution throw contour map (Fig. 16). Fault throws are used instead of total displacements because the faults in the area are steeply dipping and present a small heave; therefore the most convenient methodology from seismic data is to obtain the vertical difference (throw) between the seismic reflectors of the hanging-wall and the footwall across the fault (Cartwright et al., 1998). Twenty (20) interpreted seismic horizons were used as key markers when collecting throw data. Throw measurements were taken from seismic sections perpendicular to the strike of faults. We used an along-strike spacing of 150 m between each measurement and along-dip spacing of 25 ms. This degree of detail led to an accurate estimation of fault throws and to the completion of high-resolution fault map surfaces.

Throw-distance (T-D) plots were generated taking the maximum throw values of each fault section along the strike of the fault (Fig. 15c). These T-D plots along with coherence data and the throw surface map provide the location of different individual fault segments and their linkage. Specific throw-depth (T-Z) profiles (Fig. 14) are displayed to show the relative depth of fault initiation. Finally, all fault throw data were plotted to generate high-resolution contour throw maps in which details of the throw and fault segment interaction are observed (Fig. 16).

2.3 ICP fault and area distribution

The area of each ICP was measured from different time slices (Fig. 17) to produce a histogram displaying frequency versus ICP area (Fig. 18a). We undertook a detailed analysis to determine if there is a correlation between the size of the ICPs and the number of faults

crossing the structures as well as the number of faults surrounding the ICPs within a radius of 500m (Fig. 18b, 18c). For this analysis we took different time slices from the base Pleistocene horizon to -216 ms with a spacing of 64 ms (Fig. 17). For each ICP we counted the number of crossing faults and surrounding faults (where possible) and plotted the results in Figure 18a and 18b. These analyses are constrained by the seismic resolution. Only large-scale faults visible on seismic data were taken into account for the analysis.

3 Geological framework

3.1 Tectonic setting

The Bonaparte Basin (Fig. 1) shows a complex structural evolution; it was subject to multiple stress regimes, from predominant extension in the Paleozoic to combined compression and extension in the Mesozoic and Cenozoic. This work focuses on the Nancar Area, which is situated north of the Vulcan Sub-basin (Fig. 1). The area records different stresses that lead to a complex geological setting with rifting and compression events. During Late Paleozoic and Jurassic times, two major episodes of extension occurred (Willis, 1998). In contrast, during the Late Triassic, the Bonaparte Basin was under compressional forces (Longley et al., 2002; Saqab and Bourget, 2015a; Saqab and Bourget, 2015b).

Late Paleozoic rifting created NW-trending structures such as the Flamingo and Sahul synclines and the Londondery High (Willis, 1998). Conversely, NE-SW Jurassic extension resulted with the formation of the Malita Graben and Vulcan Sub-Basin (Willis, 1998). Late Jurassic rifting marks the onset of separation between Greater India from Western Australia, which was completed by about 132 Ma, resulting in a basin-wide Valanginian unconformity (Willis, 1998). Subsequent to the Valanginian transgression, clastic input to the basin became scarce due to flooding of the source areas (Willis, 1998). Following continental break-up, the

218 area in which the Bonaparte Basin is included became a passive margin subject to thermal
219 subsidence with maximum water depths of about 500 m in the basin depocentre (Willis,
220 1998; Longley et al., 2002; Saqab and Bourget, 2015a).

221 In the Bonaparte Basin during the Early Cenozoic, important climatic changes occurred
222 due to the progressive drift of Australasia to the north, placing the basin on a tropical latitude
223 within 30° of the Equator where carbonate factories could develop in areas with low clastic
224 input (Baillie et al., 1994; Longley et al., 2002). In the middle Eocene, a relative realignment
225 of tectonic plates gave place to a massive carbonate progradation to fill the accommodation
226 space provided by the underlying rift basins (Baillie et al., 1994). Progradational and
227 aggradational carbonate ramp settings reflect the Eocene transition phase from siliciclastic to
228 carbonate deposition (Baillie et al., 1994; Willis, 1998; Longley et al., 2002).

229 Tectonic convergence between the Australasian and SE Asian plates from the Late
230 Miocene (6 Ma) to Pliocene along the Banda Arc developed a thrust belt on Timor Island,
231 which reactivated pre-existing extensional faults as left-lateral transtensional structures
232 (Etheridge et al., 1991; Willis, 1998; Saqab and Bourget, 2015a). At present, the Timor
233 Plateau and the Banda Arc converge along the Indonesian Trough at an estimated rate of 77
234 $mm.yr^{-1}$, in a NNE direction (Ding et al., 2013; Saqab and Bourget, 2015a).

235 The main fault families (set 1) in the Bonaparte Basin have an average strike of 072˚NE
236 and the secondary fault family (set 2) strikes 050˚NE. Saqab et al (2015a) suggested that fault
237 displacement in the area occurred from Late Miocene to Early Pleistocene using the seismic
238 dataset referred therein as the Vulcan MegaSurvey. They confirmed that a good number of
239 faults terminate just below the sea floor. However, some faults did not reach Pleistocene
240 strata due to a relative quiescence in tectonic activity (Saqab and Bourget, 2015a).

241

3.2 Stratigraphic setting

Carbonate sequences in the Bonaparte Basin are recognised throughout the Cenozoic, with an onset in the Eocene (Fig. 7). The first stage of carbonate deposition records the development of a broad ramp and is characterised by a minor terrigenous input in the Early Eocene and Early Miocene (Mory, 1991; Saqab and Bourget, 2015a). This carbonate ramp succession is 3000 m thick and mainly composed of calcarenite, calcilutite and marls, with small volumes of chert in the Grebe and Oliver Formations (Fig. 7). At the base Miocene, a regional unconformity is recognised through NW Australia (Longley et al., 2002; Saqab and Bourget, 2015a) (Fig. 2). Following this event, the interaction between the Australian and Pacific plates in the mid Miocene caused a transgression which resulted in a regional flooding episode with the development of a broad carbonate shelf in the study area (Baillie et al., 1994; Whittam et al., 1996; Longley et al., 2002; Saqab and Bourget, 2015a). Periodic lowstands resulted in karstic (subaerial) erosion throughout the Miocene. At the Base of the Pliocene (Fig. 2), a local unconformity is recognised in the north Bonaparte Basin (Marshall et al., 1994; Saqab and Bourget, 2015a).

From the Late Pliocene to Early Quaternary, a tropical, wide, shallow-water platform setting dominated in the Bonaparte Basin. This led to the development of the Malita intra-shelf basin (Bourget et al., 2013). Throughout the Late Quaternary changes in the sea level occurred (Yokoyama et al., 2001). The shelf margin of the Bonaparte Basin presents a mixed system with alternating carbonate and siliciclastic sediments (Bourget et al., 2013). Saqab and Bourget (2015a) suggest that the initiation of the ICPs occurred in the Mid Pleistocene due to sea level fluctuations, oceanographic changes, and variations in the structural shaping of the margin.

3.3 Physiography

Carbonate platforms can develop along basin margins on continental shelves (Kendall and Schlager, 1981). The ICPs in the Bonaparte Basin are situated on the upper continental slope along the shelf margin (Veevers, 1971) (Fig. 1). The growth and development of ICPs could be attributed to different factors including tectonic movement, sediment supply, tectonic subsidence, relative sea level changes amongst others (Wilson, 1999; Pomar, 2001; Zampetti et al., 2004; Dorobek, 2007; Sattler et al., 2009; Ding et al., 2014). For instance, Van Tuyl et al. (2018) have shown ICPs that initiated by pinnacle reefs in the Browse Basin, further south, with pinnacles providing shallow areas for the preferential growth of ICPs.

Isolated carbonate platforms in the Bonaparte Basin have a circular and ellipsoidal morphology in plan view. Some of the most recognisable features of the ICPs in the Karmt Shoals are interior patch reefs, interplatform channels such as the ones within ICP ε and moat channels (Veevers, 1971; Saqab and Bourget, 2015a) (Fig. 3). Moats surrounding the ICPs have been interpreted by Veevers (1971) as the result of subsidence caused by the loading of the same structure over unconsolidated sediment (Fig. 3).

Different platform sizes are observed in the study area, ranging from 500 m to 18, 000 m in length. The isolated platforms are aligned along a NE-SW direction (Fig. 3). This is a similar direction to the shelf margin (Fig. 1). In bathymetric data the ICPs are observed as shallow topographic features ranging from 20 to 40 m deep (Fig. 1).

4 Seismic stratigraphy

Several seismic horizons were identified and mapped within the Karmt 3D survey. In Figure 2, seven key seismic-stratigraphic horizons are displayed, ranging in age from the Base Paleocene to the sea floor. These horizons divide Cenozoic strata into six distinct units

289 (Figs. 5 and 7). All seismic-stratigraphic surfaces were correlated with wireline data and
290 biostratigraphic data in order to constrain their ages and thickness (Figs. 5 and 6).

291

292 ***4.1 Unit 1: Early Eocene-Paleocene***

293 The lower boundary of Unit 1 coincides with horizon H_1 and comprises Early Eocene-
294 Paleocene strata (Figs. 2, 6 and 7). Horizon H_1 coincides with the Top of the Bathurst Island
295 Group, Paleocene base (Fig. 7) at a depth of 2,321.5 m in the Ludmilla-1 well (Fig. 6).
296 Horizon H_1 can only be mapped in the south of the 3D survey, as it pinches out towards the
297 north. It presents medium to low-medium positive seismic reflections. On well log data, H_1
298 shows an abrupt change in density with the highest values reaching 2.6 $g.cm^{-1}$ (Fig. 6). The
299 lowermost Unit 1 has an average thickness of 120 ms and is bounded at its top by H_2, which
300 correlates to the Top Paleocene (Fig. 7). This horizon shows a high positive amplitude and
301 pinches out against H_3 towards the north. The lower Unit 1 comprises light olive-grey
302 calcareous claystones and predominantly medium coarse grained yellow-brown and very
303 light grey calcarenites of the Johnson Formation (Willis, 1998) (Table 1). Horizon H_2 is
304 recognised on well logs as a dramatic change in density with values reaching 1.95 $g.cm^{1}$. The
305 resistivity values are also low in this lower unit, ranging from 0.2 to 4 ohm.m (Fig. 6).

306 One of the strongest positive reflections in Unit 1 is horizon H_3, which marks the top of
307 the Hibernia Formation (Fig. 7). In the Ludmilla-1 well, this reflection correlates with the top
308 of the Grebe Sandstone Member, and occurs at a depth of 1908.5 m (Fig. 6). Horizon H_3
309 marks the top of the 110 ms-thick upper Unit 1. The predominant lithology of the Grebe
310 Sandstone Member comprises a white to light grey fine sandstone (Willis, 1998) (Table 1).

311

4.2 Unit 2: Oligocene-Middle Eocene

Unit 2 has an upper boundary at the top of the base Miocene unconformity (horizon H_4), which coincides with a high to moderate positive amplitude reflection (Figs. 2 and 7). In the Ludmilla-1 well, this reflection corresponds to the top of the Cartier Formation and occurs at a depth of 1424.5 m (Figs. 6 and 7). The lower boundary of Unit 2 coincides with H_3, a Mid-Eocene unconformity. Unit 2 is a thick unit (200 ms to 550 ms) and includes the Prion Formation and the Cartier Formation (Fig. 7). Unit 2 is an interval comprising greenish grey calcareous claystones interbedded with olive-grey to yellow-grey moderately hard argillaceous calcilutites with minor yellowish-grey calcarenites (Willis, 1998) (Table 1). This interval is highly faulted across the interpreted seismic survey.

4.3 Unit 3: Miocene

The basal surface of Unit 3 corresponds to horizon H_4, whereas its top surface correlates to horizon H_5. Horizon H_5 marks the base of Pliocene strata according to biostratigraphic data and coincides with the top of the Oliver Formation at a depth of 776.5 m in the Ludmilla-1 well (Figs. 6 and 7). On seismic data, horizon H_5 is a high to moderate negative amplitude reflection easily mapped across the study area (Fig. 2). This unit is relatively thin (200-250 ms) to the south and thickens to the north, where it shows an average of 500 ms (Fig. 8). Unit 3 presents internal reflections with fairly parallel geometries and low to moderate amplitude. On wireline data, H_5 marks an abrupt change in neutron and sonic logs from relatively low values in Unit 3 to high values in Unit 4 (Fig. 6). The Oliver Formation is mainly composed of light olive-grey calcareous claystones interbedded with greenish argillaceous calcilutites and light grey, dominantly fine to medium grained arenaceous calcarenites (Willis, 1998) (Table 1).

336

337 ### *4.4 Unit 4: Pliocene*

338 Unit 4 is bounded by the base Pliocene (H_5) and base Pleistocene (H_6) horizons (Figs. 2
339 and 7). The base Pleistocene (H_6) is marked by a high-amplitude, positive reflection at a
340 depth of approximately 561.5 m in the Ludmilla-1 well (Figs. 6 and 7). Strata in this unit
341 consist of light olive grey calcareous claystones (Willis, 1998) (Table 1). Unit 4 comprises
342 the Barracouta Formation and varies in thickness from 100 to 350 ms, thickening towards the
343 NW (Fig. 8).

344

345 ### *4.5 Unit 5: Pleistocene*

346 On the interpreted seismic sections, the top of Unit 5 coincides with the modern
347 seafloor at 220 m in the Ludmilla-1 well (Fig. 6). This Pleistocene unit varies in thickness
348 from 200 to 450 ms in areas with no ICPs (Fig. 8). Close to ICPs, where thicker intervals are
349 present, the unit varies in thickness from 450 to 650 ms (Figs. 2 and 8). The base of the unit
350 is horizon H_6, which also coincides to the base of most ICPs. The interior of Unit 5 is
351 composed of high-amplitude reflections (Fig. 7). Seismic reflections below the ICPs are not
352 continuous, suggesting a change in facies. The seismic response within these areas is
353 characterised by mounded morphologies and internally chaotic to stratified reflections from
354 the margins to the ICPs internal structure, as expected for carbonate platform facies (Burgess
355 et al., 2013). Unit 5 comprises the Alaria Formation, which consist of yellowish-grey coarse-
356 grained calcarenites interbedded with silty calcilutites (Willis, 1998) (Table 1).

357 The internal reflections of the biggest ICP ε present clinoforms suggesting the
358 coalescence of smaller individual ICPs into a larger feature (Figs. 9 and 19).

359

5 ICP geometries and fault distribution

Within the study area, there are 51 Quaternary ICPs with different sizes, ranging in area from 0.1 km^2 to 200 km^2 (Figs. 9, 17 and 18a). The histogram in Fig. 18a shows a multimodal distribution of platform areas with three different peaks. This is an indicator that there are three groups of ICPs with different areas. The first peak shows a group of ICPs with an area of around 0.2 km^2, the second peak shows the major frequency with ICP areas of 2 km^2; and a third peak shows a distribution of ICPs with an area of 20 km^2. The higher frequency of ICPs is located within the scale range of 2 km^2. The smaller ICPs are concentrated in the frequency peak of a range of sizes with the order of 0.2 to 0.3 km^2. The biggest ICP (ε) has an area of about 189 km^2.

The relationship between the ICP area and the faults as indicated by the scatter plots (Fig. 18b, 18c) suggests that there is no spatial correlation with regards to the ICP size and the number of faults that cross these structures or surround them. However, the ICPs in the Bonaparte Basin have a sub-circular and ellipsoidal morphology in map view, with a NE long-axis direction that is similar to the orientation of underlying faults (Figs. 3 and 9).

It is observed from the seafloor map (Fig. 3) and seismic sections (Figs. 11, 12 and 13) of the Karmt shoals that the current ICPs could have been the result of the coalescent evolution of smaller platforms. For instance, the large platform ε is observed as an elongated feature with two main branches (Fig. 9); this suggests coalescence of smaller platforms. In section view (Fig. 12) the platform interior is characterised by clinoforms, which also indicates the merging and aggradation of ICPs. Similar examples previously described include the isolated platforms of the East Natuna Basin (Bachtel et al., 2004) and offshore Madura, Indonesia (Posamentier et al., 2010).

A detailed structural interpretation of the base Pleistocene (H_6) using an extracted coherence attribute resulted in the sub-division of the study area into four distinct zones (Fig. 9). These zones were defined based on the size, clustering, position and geometry of the ICPs, as well as the type, density, and orientation of interpreted faults.

5.1 Zone 1

Zone 1 occurs to the northwest of the study area (Fig. 9). This zone is mainly characterised by the absence of ICPs. Zone 1 presents a high density of Plio-Pleistocene normal faults striking NE. The faults have synthetic and antithetic structures that are closely spaced (100-300 m) (Fig. 12). These faults do not propagate to the surface.

5.2 Zone 2

Zone 2 covers an area aligned NE-SW, just to the south of zone 1 and comprises the large platform ε together with 14 smaller isolated platforms (Fig. 9). Plio-Pleistocene normal faults strike NE-SW with an average of 072° (Figs. 11, 12 and 13). The large isolated platform ε includes large fault zones with a net normal offset, such as F6 and F7, that cross cut the platform as a later event (Figs. 9 and 19b, 19c). In contrast, to the NE the interior of the ICP ζ is intact, and bounded by a fault system that includes F5 (Fig. 9).

5.3 Zone 3

Zone 3 is located to the south of Zone 2, and comprises a large number of ICPs (28). Fault transect F1 is contained in this area (Figs. 9 and 13). There are two fault families in this area; the principal family striking 072°NE (fault transects F1, F3 and F4) and a secondary

family striking around 050°NE (fault transect F3). The interaction between faults creates large relay ramp structures, such as the one containing ICP η, which is bounded by faults F1, F2 and F3 (Fig. 9).

5.4 Zone 4

Zone 4 occurs to the southeast of the study area (Fig. 9) and it is mainly characterised by its relative scarcity of ICPs. There are only eight small ICPs, including ICP θ with an average area of 1.5 km^2. This zone presents a major fault zone around fault F8 (Fig. 12).

6 Fault throw analysis

In order to better understand the propagation history of the interpreted faults, maximum throw measurements were taken from Fault F1 (Figs. 14 and 15). This fault was selected for our analysis because it crosses four different ICPs (α, β, γ, δ).

Fault throw measurements were completed in detail, every 150 m along the strike of the faults, and every 25 ms along their dip. With these measurements, we generated detailed throw-depth (T-Z) plots as well as a maximum throw-distance (T-D) plot (Figs. 14 and 15c). The large amount of data was compiled to generate a high-resolution map of throw displacement (Fig. 16).

T-Z profiles are useful to provide the style, timing of fault initiation and the detailed kinematic history of normal faults (Hongxing and Anderson, 2007). Overall, the intention is to analyse the slope of different curve segments and their deflections within the throw profile. Our analyses were based on the conceptual models developed by Hongxing and Anderson (2007). A vertical line segment with a constant throw indicates a simple postdepositional

fault, cutting the entire prekinematic stratigraphic section; it suggests that it was formed after all the sedimentary layers were deposited. Another way to determine the presence of a postdepositional fault is by a constant growth index of 1.0 for all layers because there is no change in the thickness of the strata.

On the other hand, a T-Z profile with a positive slope and throw values decreasing at depth towards the older units, indicates a postdepositional keystone-stretching fault, where the fault propagates downwards, having the uppermost and youngest units with the largest throw values. The growth index of postdepositional stretching faults is also identified by a constant value of 1.0 or less, due to the thinning of the layers by stretching. The timing of fault formation post-dates the deposition of the unit recording the largest fault throw (Hongxing and Anderson, 2007).

In the scenario that the T-Z profile presents a negative slope, with throw values increasing towards the older units, the presence of a syndepositional normal growth fault is recognised. The sedimentary sections expand in the hanging wall, leading to a change in the growth index with values greater than 1.0 (Hongxing and Anderson, 2007).

The combination between throw profiles and growth index are useful to provide information of the time in which a fault first nucleates (Hongxing and Anderson, 2007). A change from postdepositional keystone-stretching fault to a growth syndepositional fault is given by the deflection of a positive slope curve to a negative curve. The growth index profile in this case, shows a change in values from 1.0 or less to values greater than 1.0. The maximum throw value in the profile along with the change of the growth index corresponds to the initiation of the fault growth (Hongxing and Anderson, 2007).

Several seismic sections were analysed with T-Z profiles in order to determine the growth history of the fault transect F1 (Fig. 14). Across the study area, the results suggest that

453 there are two fault displacement stages throughout the Cenozoic. The stages are identified as
454 Paleogene faulting, with a maximum throw recorded of 255 ms TWT, and Neogene-
455 Quaternary faulting with a maximum throw of 200 ms TWT (ca. 287 m and 225 m
456 respectively, assuming an average velocity of 2250 $m.s^{-1}$) (Fig. 14).

457 Fault throw values in Unit 1 decrease towards its base (Fig. 14). This segment of the
458 throw profile has a positive slope and the growth index presents values less than 1.0,
459 indicating that Unit 1 was deposited before faulting commenced (Fig. 14). Unit 1 is
460 considered as a prekinematic layer. The maximum throw values are observed around the Mid
461 Eocene horizon (H_3). Above this throw maxima, within Unit 2, throw values start to decrease
462 towards younger strata (Fig. 14b, 14d, 14f and 14h). The throw profile in this segment has a
463 negative slope and growth index values are greater than 1.0 (Fig. 14). The change in
464 deflection from positive slope to negative slope, in addition to the change of growth index
465 values from less than 1.0 to greater than 1.0, suggest a change from postdepositional faulting
466 to syndepositional faulting. These two faulting stages are considered to be the Paleogene
467 faulting (Fig. 14).

468 Fault throw and growth index values are observed to remain relatively constant around
469 the base Miocene horizon (H_4) within the uppermost part of Unit 2 and the lowermost part of
470 Unit 3 (Fig. 14b, 14d and 14h). This can be interpreted as a period of fault inactivity in the
471 area. A change is observed upwards with a positive slope throw profile with values
472 progressively increasing towards the uppermost part of Unit 3, around the base Pliocene
473 horizon (H_5) (Fig. 14b, 14f). The growth index profile records values less than 1.0. This
474 segment of the throw profile records prekinematic strata. This stage is considered to reflect
475 postdepositional faulting due to the cessation of activity of the Paleogene faulting.

476 A second throw maximum is recognised in mid Late Miocene to Early Pliocene strata
477 around the horizon H_5 (Fig. 14). This throw maximum indicates the start of the second

faulting period described here as the Neogene-Quaternary faulting. Above this maximum, it is observed that the throw values start to decrease towards Quaternary strata, recognised from the throw profiles as a negative slope line (Fig. 14b, 14d, 14f, 14h). In this segment of the profile, growth index values are greater than 1.0, suggesting thicker strata in the hanging-wall, characteristic of a syndepositional normal growth fault. In some areas (Fig. 14a, 14g), the growth fault propagates to the sea floor. However, below the ICPs, fault throw decreases and stops before reaching the sea floor (Fig. 14c, 14e). The presence of growth faults and the thickening of the hanging-wall strata in Units 4 and 5 (Fig. 14a, 14c, 14e, 14g) confirm the occurrence of a syndepositional fault. This suggests that at the time of initiation of the ICPs (Quaternary), the faults were still propagating to the surface. The fact that the fault does not completely cross-cut the platform indicates that carbonate productivity was higher than vertical fault propagation rates.

The T-D plot in Figure 15 shows the maximum fault throw values along the strike of fault transect F1 for the Neogene-Quaternary. It shows different maximum peaks along the fault transect, which is indicative of the presence of different individual fault segments within fault transect F1 (Fig. 15b, 15c). These fault segments are indicated by red solid lines in Figure 15c along the fault throw maxima (yellow line). A dashed line was drawn as the interpretive extension of each fault segment. It is interpreted that lateral and vertical propagation of these individual fault segments throughout the time led to soft linkage between their fault tips, creating relay ramps. In these relay ramps there is a transfer of displacement from the footwall to the hanging-wall. The relay ramps are situated in areas with relative minimum displacement between one segment and another. These relay ramps are shown in Figure 15c as pink rectangle areas. These linked fault segments created a large fault transfer zone along fault F1 (Larsen, 1988; Fossen and Rotevatn, 2016). This type of fault interaction exists at different scales of observation (Fig. 9). In the study area, there are

503 relatively small relay ramps (2 km wide) created by individual fault segments, such as the one
504 located around the ICP α (Fig. 15). Moreover, there are larger relay ramp structures (>10 km
505 wide) created by the interaction between large fault transects such as the relay ramp between
506 fault transects F1 and F2 (Figs. 9 and 19).

507 Relay ramps can only be observed on seismic if the ramp is large enough to be clearly
508 imaged in such seismic resolution (e.g. the relay ramp containing the ICP α, shown as a light
509 purple polygon with a red outline in Figure 9b). Relay ramps that are less than 1 km wide,
510 due to their small size, are not easily recognised on the seismic at first sight. For this reason,
511 it is necessary to use the T-D plot to accurately identify relay ramps, such as those in ICP γ,
512 which are only clearly recognised from the T-D plot due to the short throw values between
513 the fault segments (Fig. 15c). For the relay ramps that can be clearly identified in a seismic
514 section, they present rotation of strata between the two linked faults (e.g. F1a and F1b),
515 where the strike and dip of the beds are slightly different to the general orientation (Fig. 15d,
516 15e). Relay ramps can be identified from the T-D plot in Figure 15c as the intersection
517 between two different fault segments (pink areas), usually occurring in areas with low throw
518 values. Relay ramp structures are not only seen in fault transect F1, but in some other parts of
519 the study area (Fig. 9). There are some small relay ramps that are placed close to the large
520 fault structures, such as the ones shown in Figure 9b displayed as light purple polygons with
521 a red outline. There are also some other larger ramps shown as light pink polygons on the
522 map (Fig. 9b), such as the one containing ICP η.

523 Fault throw measurements of about 200 T-Z plots taken along the fault transect F1 were
524 used to generate a high-resolution fault throw map (Fig. 16). Unlike in the T-D plot (Fig. 15c)
525 the geometry of the individual fault segments can be determined as well as the depth of the
526 fault's nucleation. The fault throw surface map shows the elliptical-like geometry of the fault
527 segments (white ellipses in Fig. 16). The maximum throw is localised inside the fault

528 segment (warm colours) suggesting fault initiation (Cartwright et al., 1998; Hongxing and
529 Anderson, 2007). The throw values decrease towards the fault tips (cold colours) (Muraoka
530 and Kamata, 1983). One example is seen at about 22 500 m along strike, where there is an
531 area of high throw around horizon H_3. The fault throw values decrease laterally and vertically
532 from about 240 ms (orange colour) in the core of the fault segment to lower values of about
533 130 ms (yellow and green colours) towards the fault tips.

534 Similar to the T-D plot, relay ramps can be interpreted in the areas where the two fault
535 tip segments interact and present relatively low throw values. These relay ramp areas are
536 plotted as pink zones on the fault throw map, such as the relay ramp between the fault
537 segments 1a (F1a) and 1b (F1b) (Fig. 16).

538 The presence of two faulting events is clearly recognised in the T-Z plots (Fig. 14) and the
539 fault throw map (Fig. 16). The Paleogene fault segments are observed below horizon H_4
540 between -2000 and -1500 ms TWT (Fig. 16). The Neogene-Quaternary faulting event is
541 observed with fault segments mostly above H_4.

542

543 **7 Fault propagation styles**

544 In the study area, Paleogene and Neogene faults are NE striking (Fig. 9). They have a
545 net normal component. The fault network presents individual fault segments linked to each
546 other (Fig. 9). The linkage and overlap between several fault segments results in the creation
547 of large fault transects, which is known as geometric coherence. The displacement of each
548 fault segment accumulates and creates a large fault (Walsh and Watterson, 1991; Conneally
549 et al., 2014). The formation of the fault transects F1 to F8 present geometric coherence (Fig.
550 9).

Around fault transect F1, within the overlap zones between different fault segments, small relay ramps are observed primarily from T-D plots and the throw surface map as well as large relay ramps easily identified in the variance map (Figs. 9, 15 and 16). In Figure 15, where ICP α is located, there is an intact relay ramp with a maximum width of about 2 000 m.

The interaction of several fault segments can create a large fault, e.g. fault transect F1. These long faults, if interpreted on a regional scale as one large fault, can interact with other large fault transects. The interaction of the faults function in a similar way to individual fault segments. As a result, they can generate extensive areas of a relay ramp such as the 8 km wide relay ramp between F1, F2 and F3 containing the ICP η (Fig. 9). The relay block normally presents considerable bed rotation and breached deposits even if it is not visible in seismic resolution (Fossen and Rotevatn, 2016). We suspect that this uneven paleo-surface could be a good foundation for the initiation of ICPs based on the fact that all the ICPs that are cut by fault F1 directly correlate to the position of an underlying relay ramp. However, direct spatial relationship between most relay ramps and the position of ICPs has not been identified.

8 Discussion

8.1 Relationship between carbonate deposition and fault growth

In the Bonaparte Basin, there is a high concentration of ICPs across the shelf margin (Fig. 1). The area is highly faulted as observed with coherence attribute maps (Fig. 9). Fault throw data suggests correlation with the position of linked fault segments and associated relay ramps (Figs. 15 and 16). Despite the lack of spatial relationship, some of the ICPs such

575 as α, β, γ, δ, ε, ζ, η and θ correlate with the locus of an underlying relay ramp as
576 demonstrated in the T-D plot (Fig. 15c) and the fault throw map (Fig. 16). For this reason, the
577 concept of fault throw analysis is introduced as an additional aspect to take into consideration
578 when identifying ICPs where there is an extensional setting (Burgess et al., 2013; Rusciadelli
579 and Shiner, 2018) and to generate different models of ICPs when the faults interact with their
580 growth or their subsequent development.

581 The initiation of the ICPs in the Timor Sea has been attributed to antecedent
582 topography that was able to trigger the preferential settlement of reef building organisms, and
583 thus controlled the distribution of isolated carbonate platforms in the Vulcan Sub-Basin
584 (Saqab and Bourget, 2015a). This antecedent topography is tectonic-related due to the
585 extensional faulting in the area. It is well documented in the literature that ICPs can start on a
586 structural high with a horst-like structure, such as the ICPs in the Maldives Archipelago
587 (Paumard et al., 2017). Saqab and Bourget (2015a) have documented the development of the
588 "Big Bank" in an adjacent area to the Karmt Shoals. This ICP was interpreted by the latter
589 authors as to be controlled by a structural high. However, as recognised from our 3D seismic
590 dataset, there are some scenarios in which ICPs do not grow on structural highs (Fig. 9). In
591 this work we try to extend the understanding of fault controls on ICPs where they are not
592 exactly on structural highs, but are crosscut by faults.

593 As recognised from the T-D profile (Fig. 15c) and the fault throw map (Fig. 16), the
594 ICPs in fault transect F1 (α, β, γ and δ) are underlain by different relay ramps formed by the
595 interaction of the fault tips between two fault segments. These relay ramps produce local bed
596 rotation (Giba et al., 2012) that creates a change in topography. The gradual transition from
597 intact rock to a breached relay ramp develops fractures in the area, even before the two
598 interacting faults are completely breached (Fossen and Rotevatn, 2016). Fossen and Rotevatn
599 (2016) have shown a field example from the Canyonlands National Park, USA, in which the

ramp is highly fractured. Therefore it is probable to have a high concentration of fractures in the sub-seismic scale even if the ramp appears to be continuous and unbreached in the seismic data, as it is not fully imaged on the seismic due to its resolution. This uneven topography may then favour the concentration of opportunist biota and result in the initiation of ICPs (Fig. 20). However, this correlation between relay ramps and the development of ICPs is not a direct relationship. Nevertheless it is a way to explain the control of some ICPs. Transfer zones including relay ramps (soft-linkage) are known to be important features in controlling basin stratigraphy due to the marked change in relief in both hanging wall and footwall associated to the transfer zones (Leeder and Gawthorpe, 1987; Gawthorpe and Hurst, 1993). The Abu Shaar el Qibli carbonate platform in the Gulf of Suez is an example of an ICP positioned on a transfer zone (Gawthorpe and Hurst, 1993; Cross et al., 2008).

Based on our analysis, we observed three scenarios in which faults interact to trigger the initiation and development of ICPs: (1) interaction of single fault segments and the creation of relay ramps (Figs. 19 and 20a, 20b); (2) large scale relay ramps created by large fault transects (Figs. 19 and 20c); and (3) structural highs (Fig. 19). Furthermore, the ICPs can start on different places of the relay ramp: (1) close to the fault tips (α, Figs. 15 and 20a) or (2) inside the relay ramp (η, Figs. 15 and 20b).

Three distinct models explaining carbonate platform growth are proposed here based on the comparison between productivity- and fault throw- rates. (1) one in which fault throw is larger than carbonate productivity (Figs. 19f, 19g and 21); (2) a second model considering fault throw to be equal or less than carbonate productivity (Figs. 19d, 19e and 21); and (3) a third model in which fault throw post-dates the growth of the carbonate platform(s) (Figs. 19b, 19c and 21).

In our study area, the three types of models are present. The type 1 can be seen in zone 2 with platforms presenting intact internal structure since no faults cross-cut the structures

(Fig. 19f, 19g). These ICPs developed in the structural high bounded by faults F1 and F4. There is a cluster of isolated platforms within this block including ICP δ. Type 2 ICPs can also be found within the zone 2. An example of a type 2 platform developed inside of a ramp is shown in Figure 19d, where the faults F1 and F2 created a large ramp with a wide rotational surface suitable for the development of the ICP η. A type 2 platform developed between the fault tips of two different individual fault segments is shown in Figure 19e. This type of platform is characterised as faulted in its interior, as observed in the seismic line. The type 3 ICPs are characterised by the post growth faulting. The faults propagate after the growth and deposition of the ICPs, such as in the ICP ε faulted by several faults, including faults F6 and F7 (Figs. 19b, 19c and 21). This ICP ε is observed as type 2 to the northeast (Fig. 19c) in which the syn-depositional fault propagates to the surface. In the same area of the ICP ε it is also recognised a shallow fault that was developed after the ICP growth, implying a type 3 ICP.

8.2 Implications for petroleum systems on continental margins

ICPs are well-known as good targets for reservoirs containing significant accumulation of hydrocarbons. It is estimated that around 50 billion barrels of oil equivalent reserves are accumulated within isolated carbonate platforms around the world (Greenlee et al., 1993). Several super-giant fields are found in ICPs such as the Tengiz and Kashaghan fields in the Precaspian Basin (Kuznetsov, 1997). Another benefit of the ICPs is that several petroleum system elements can be easily identified in seismic. Because of their geometry, the trap and seal properties are favourable with a four-way dip closure; normally well sealed by fine-grained marine strata or evaporites (Burgess et al., 2013). Sideways, adjacent or underlying strata can form good source rocks with a clear migration pathway and migration focus into

649 the ICP trap (Burgess et al., 2013). However, not all the ICP structures have the same
650 potential and volume capacity to store hydrocarbons. For this reason, it is critical to not just
651 identify the ICP structures, but to perform a broader evaluation before deciding where is the
652 best structure to drill and increase the probability to get an exploration success.

653 It is known in the literature that relay ramps represent potential pathways for vertical
654 migration fluids (Fossen and Rotevatn, 2016). Relay ramps can enhance vertical porosity and
655 permeability due to a range of fluid-rock interactive process. The breaching within the relay
656 structure, can develop a fracture system that enhances porosity and permeability (Fossen and
657 Rotevatn, 2016). Furthermore, during the relay development and breaching, the faults can
658 create compartmentalised blocks that can generate different isolated reservoirs. One example
659 is the Gullfaks Field in the northern Sea (Fossen and Hesthammer, 1998; Fossen and
660 Rotevatn, 2016). These structures can serve as vertical pathways for fluid migration and
661 hydrocarbon accumulation (Fossen and Rotevatn, 2016). Therefore we can predict that ICPs
662 located over relay ramps are good reservoir targets since they make an attractive scenario for
663 hydrocarbon migration and trapping. The hydrocarbon can migrate through the relay ramp
664 and then store within the platform.

665 The ICP strata is recognised to present an early cementation, leading to a rigid structure
666 (Burgess et al., 2013). The early cementation of the platform can lead to a significant
667 development of small-scale faults and fractures with the syn-tectonic deposition of the
668 platform (Cross et al., 2008). Therefore we can infer that the ICPs with syn-tectonic growth
669 such as the ones corresponding to the type 2 model proposed herein may have a constant
670 fracturing on the platform interior due to the syn-depositional growth of the platform during
671 the upwards fault propagation growth. Similarly, the type 3 model ICPs may develop fracture
672 networks in their interior as the fault propagates to the platform interior. This induced

673 fracturing could develop a secondary porosity within the platform structure that signifies an
674 enhanced reservoir capacity (Cross et al., 2008).

675 Based on our analysis of ICPs in the Karmt Shoals we propose that in exploration of
676 new prospects, once the isolated carbonate platforms are identified from seismic data, one
677 way to discriminate which ICP possesses the best scenario to be a hydrocarbon reservoir is by
678 identifying the ICPs that are positioned on a relay ramp. In accordance with the models
679 proposed, the ICP with a higher confidence of success would be found in type 2 and 3 models
680 (Fig. 21). The type 2 and 3 ICPs are developed on a relay ramp, which may facilitate the
681 hydrocarbon migration towards the ICP interior. Furthermore, the structure interior should be
682 highly fractured due to the syn- and post- depositional faulting, leading to an enhanced
683 volume capacity to store hydrocarbons.

684 Tectonism is well documented in many geological settings from 2D and 3D seismic
685 data as well as from outcrop analysis to be a mechanism that influence the location, growth
686 and demise of ICPs around the world. The most common configuration is related to
687 topographic highs created by the uplift of blocks bounded by faults, named as fault-block
688 carbonate platforms in Bosence (2005). Late Oligocene-Early Miocene carbonate platforms
689 from the Maldives Archipelago are described to be controlled by structural highs (Paumard et
690 al., 2017). Another major example is the Miocene Luconia province, where reefs grow on
691 prominent fault blocks (Zampetti et al., 2004; Rosleff-Soerensen et al., 2016).

692

693

694

9 Conclusions

Fault throw measurements taken from 3D seismic data allow the creation of detailed throw-depth (T-Z) and throw-distance (T-D) profiles as well as a high resolution fault throw displacement surface. These profiles and maps along with well data are the basis to analyse the timing of fault initiation and fault growth evolution.

The Cenozoic in the Vulcan Sub-Basin presents two stages of faulting: the Neogene/Quaternary faulting and the Paleogene faulting, which are observed as throw maximas from the T-Z plots (Fig. 14) and throw surface map (Fig. 16). A period of fault inactivity between these faulting stages is recognised from the Late Oligocene to Early Miocene.

The development of ICPs based on the Karmt3D seismic data, suggest their initiation from the beginning of Unit 5 onwards. However, Saqab and Bourget (2015a) mention that the ICP development started during the Mid Pleistocene. Paleo-topographic discontinuities in the Pleistocene are attributed to the fault displacement and the related deformation of the seafloor, generating structures such as relay ramps and structural highs. As recognised from the distribution analysis of ICPs versus faults (Fig. 18), the majority of the ICPs does not have a direct relation to the faults. However, some of the ICPs (e.g α, β, γ and η) relate to the position of relay ramps underneath. For these examples, relay structures play a very important role in the initiation and development of ICPs.

Three different models were presented showing the relationship between ICPs and fault linkage and distribution: (1) one in which fault throw is larger than carbonate productivity; (2) a second model considering fault throw to be equal or less than carbonate productivity; and (3) a third model in which fault throw post-dates the growth of the carbonate platform(s).

718 The models proposed herein are useful as analogues for the hydrocarbon prospectivity
719 evaluation of ICPs in extensional settings in the subsurface. The recognition and comparison
720 of an ICP using 3D seismic data and the given models can lead to the prediction of the
721 structure with a greater hydrocarbon migration and volume capacity. The type 2 and 3 ICPs
722 present the best scenarios for hydrocarbon prospectivity. They present a favourable
723 hydrocarbon migration pathways (relay ramp) and structural traps (platform facies), which
724 can be highly fractured, providing an important degree of enhanced (secondary) porosity. We
725 expect that these models can be applied to similar settings on equatorial margins around the
726 world to facilitate the identification of new prospect targets.

727

728 **10 Acknowledgments**

729 The work contained in this paper is part of a PhD research supported by the Mexican
730 National Council of Science and Technology (CONACYT) as well as the hydrocarbon
731 Secretariat of Energy (SENER). We are thankful to Geoscience Australia to provide the
732 Karmt 3D seismic volume in addition to well data utilised in this work. We acknowledge
733 Schlumberger (Petrel®) for granting academic licenses to Cardiff's 3D Seismic Lab. The
734 original manuscript has benefited considerably from thoughtful and appropriate comments
735 and criticisms from reviewers Peter Burgess and Dan Bosence.

736

737

738

739

740

11 References

Alsharhan, A.S. 1987. Geology and reservoir characteristics of carbonate buildup in giant Bu Hasa oil field, Abu Dhabi, United Arab Emirates. *AAPG Bulletin* 71(10), pp. 1304–1318.

Alves, T.M. et al. 2006. MesozoicndashCenozoic evolution of North Atlantic continental-slope basins: The Peniche basin, western Iberian margin. *AAPG Bulletin* 90(1), pp. 31–60. Available at: http://search.datapages.com/data/doi/10.1306/08110504138 [Accessed: 9 October 2018].

Alves, T.M. 2016. Polygonal mounds in the Barents Sea reveal sustained organic productivity towards the P-T boundary. 28, pp. 50–59. Available at: https://onlinelibrary.wiley.com/doi/pdf/10.1111/ter.12190 [Accessed: 12 November 2018].

Bachtel, S.L. et al. 2004. *Seismic Stratigraphic Evolution of the Miocene-Pliocene Segitiga Platform, East Natuna Sea, Indonesia: The Origin, Growth, and Demise of an Isolated Carbonate Platform*. Available at: https://pubs.geoscienceworld.org/books/chapter-pdf/3814998/9781629810058_ch14.pdf [Accessed: 12 March 2019].

Baillie, P.W. et al. 1994. The tectonic framework of Western Australia's Neoproterozoic to Recent Sedimentary Basins. *The Sedimentary Basins of Western Australia: Proceedings of the Petroleum Exploration Society of Australia,* , pp. 45–62.

Blendinger, W. et al. 1997. Carbonate buildup flank deposits: an example from the Permian (Barents Sea, northern Norway) challenges classical facies models. *Sedimentary Geology* 112(1–2), pp. 89–103. Available at: https://www.sciencedirect.com/science/article/pii/S0037073897000250 [Accessed: 12

764 November 2018].

765 Borromeo, O. et al. 2010. Stratigraphic Architecture of the Early Carboniferous
766 Reservoir in Karachaganak Field, Pri-Caspian Basin (Kazakhstan). In: *SPE Caspian Carbonates*
767 *Technology Conference*. Society of Petroleum Engineers. Available at:
768 http://www.onepetro.org/doi/10.2118/139887-MS [Accessed: 19 October 2018].

769 Bosence, D. 2005. A genetic classification of carbonate platforms based on their
770 basinal and tectonic settings in the Cenozoic. *Sedimentary Geology* 175(1–4), pp. 49–72.
771 Available at: https://www.sciencedirect.com/science/article/pii/S0037073805000370
772 [Accessed: 4 March 2019].

773 Bourget, J. et al. 2013. Origin of Mixed Carbonate and Siliciclastic Sequences at the
774 Margin of a "Giant" Platform During the Quaternary (Bonaparte Basin, nw Australia). In:
775 *Deposits, Architecture, and Controls of Carbonate Margin, Slope and Basinal Settings*. SEPM
776 Society for Sedimentary Geology, pp. 157–177. Available at:
777 https://pubs.geoscienceworld.org/books/book/1970/chapter/11875239/ [Accessed: 13
778 February 2018].

779 Brown, A.R. 2011. *AAPG Memoir 42. Interpretation of three-dimensional seismic data*.
780 Seventh. Tulsa, Oklahoma, U.S.A.: Society of Exploration Geophysicists and American
781 Association of Petroleum Geologists. doi: https://doi.org/10.1306/M4271346.

782 Buarque, B. V et al. 2017. Carbonate Buildups in the Pernambuco Basin, NE Brazil. *An*
783 *Acad Bras Cienc* 89(2), pp. 841–857. Available at: http://dx.doi.org/10.1590/0001-
784 3765201720160544www.scielo.br/aabc [Accessed: 12 November 2018].

785 Burgess, P.M. et al. 2013. Methods for identification of isolated carbonate buildups
786 from seismic reflection data. *AAPG Bulletin* 97, pp. 1071–1098. Available at:

787 http://archives.datapages.com/data/bulletns/2013/07jul/BLTN12011/IMAGES/BLTN12011.
788 PDF [Accessed: 7 February 2018].

789 Carenzi, G. and Cazzola, L. 2008. *Final Report - AC/P-38 Time and Depth Re-processing*
790 *Report 3D Karmt Seismic Survey*.

791 Cartwright, J. et al. 1998. Polycyclic motion history of some Gulf Coast growth faults
792 from high-resolution displacement analysis. *Geology* 26(9), p. 819. Available at:
793 https://pubs.geoscienceworld.org/geology/article/26/9/819-822/206979 [Accessed: 2 May
794 2019].

795 Catuneanu, O. 2006. *Principles of sequence stratigraphy*. Elsevier.

796 Chopra, S. and Marfurt, K.J. 2007. *Seismic attributes for prospect identification and*
797 *reservoir characterization*. Society of Exploration Geophysicists and European Association of
798 Geoscientists and Engineers.

799 Collins, J. et al. 2006. Facies and reservoir-quality variations in the late Visean to
800 Bashkirian outer platform, rim, and flank of the Tengiz buildup, Precaspian Basin,
801 Kazakhstan. *P.M. Harris and L.J. Weber, eds., Giant hydrocarbon reservoirs of the world:*
802 *From rocks to reservoir characterization and modeling: AAPG Memoir 88/SEPM Special*
803 *Publication* , pp. 55–95. Available at: https://www.researchgate.net/publication/282852637
804 [Accessed: 4 March 2019].

805 Collins, J.F. et al. 2016. *Origin of the Raised Rim in the Kashagan Buildup, Kazakhstan:*
806 *A Hypothesis for Diagenesis Associated With Fractures and Burial Compaction**. Available at:
807 http://www.searchanddiscovery.com/documents/2016/20365collins/ndx_collins.pdf
808 [Accessed: 12 November 2018].

809 Conneally, J. et al. 2014. Contrasting origins of breached relay zone geometries.
810 *Journal of Structural Geology* 58, pp. 59–68. Available at:
811 https://www.sciencedirect.com/science/article/pii/S0191814113001855?via%3Dihub
812 [Accessed: 28 August 2018].

813 Cross, N.E. et al. 2008. Tectono-sedimentary models for rift-basin carbonate systems.
814 *Controls on Carbonate Platform and Reef Development, SEPM, Special Publication* 89, pp.
815 83–105. Available at: https://www.researchgate.net/publication/283998921 [Accessed: 21
816 March 2019].

817 Ding, W. et al. 2014. Carbonate Platforms in the Reed Bank Area, South China Sea:
818 Seismic Characteristics, Development and Controlling Factors. *Energy Exploration &*
819 *Exploitation* 32(1), pp. 243–261. Available at:
820 http://journals.sagepub.com/doi/10.1260/0144-5987.32.1.243 [Accessed: 12 November
821 2018].

822 Ding, X. et al. 2013. Indonesian Throughflow and monsoon activity records in the
823 Timor Sea since the last glacial maximum. *Marine Micropaleontology* 101, pp. 115–126.
824 Available at: https://www.sciencedirect.com/science/article/pii/S0377839813000157
825 [Accessed: 12 February 2018].

826 Dorobek, S. 2007. Carbonate-platform facies in volcanic-arc settings: Characteristics
827 and controls on deposition and stratigraphic development. In: *Formation and Applications of*
828 *the Sedimentary Record in Arc Collision Zones*. Geological Society of America Special Paper
829 436. Available at: https://www.researchgate.net/publication/284141450 [Accessed: 4
830 March 2019].

831 Elliott, S. et al. 1998. The giant Karachaganak field, unlocking its potential. *Oilfield*

Review 10(3), pp. 16–25.

Elvebakk, G. et al. 2002. From isolated buildups to buildup mosaics: 3D seismic sheds new light on upper Carboniferous–Permian fault controlled carbonate buildups, Norwegian Barents Sea. *Sedimentary Geology* 152(1–2), pp. 7–17. Available at: https://www.sciencedirect.com/science/article/pii/S0037073802002324 [Accessed: 12 November 2018].

Etheridge, M. et al. 1991. The role of intraplate stress in tertiary (and mesozoic) deformation of the Australian continent and its margins: A key factor in petroleum trap formation. *Exploration Geophysics* 22(1), p. 123. Available at: http://www.publish.csiro.au/?paper=EG991123 [Accessed: 12 February 2018].

Fossen, H. and Hesthammer, J. 1998. Structural geology of the Gullfaks Field, northern North Sea. *Geological Society, London, Special Publications* 127(1), pp. 231–261. Available at: http://sp.lyellcollection.org/lookup/doi/10.1144/GSL.SP.1998.127.01.16 [Accessed: 28 August 2018].

Fossen, H. and Rotevatn, A. 2016. Fault linkage and relay structures in extensional settings—A review. *Earth-Science Reviews* 154, pp. 14–28. Available at: http://www.sciencedirect.com/science/article/pii/S0012825215300738 [Accessed: 29 November 2017].

Gawthorpe, R.L. and Hurst, J.M. 1993. Transfer zones in extensional basins: their structural style and influence on drainage development and stratigraphy. *Journal of the Geological Society* 150(6), pp. 1137–1152. Available at: http://jgs.lyellcollection.org/lookup/doi/10.1144/gsjgs.150.6.1137 [Accessed: 25 March 2019].

Giba, M. et al. 2012. Segmentation and growth of an obliquely reactivated normal fault. *Journal of Structural Geology* 39, pp. 253–267. Available at: http://www.sciencedirect.com/science/article/pii/S0191814112000132?via%3Dihub#fig1 [Accessed: 9 January 2018].

Greenlee, S.M. et al. 1993. Stratigraphic framework of productive carbonate buildups. *Carbonate sequence stratigraphy: recent developments and applications: AAPG Memoir* 57, pp. 43–62.

Hongxing, G. and Anderson, J.K. 2007. Fault throw profile and kinematics of Normal fault: conceptual models and geologic examples. *Geological Journal of China Universities* 13, pp. 75–88.

Hutchison, C.S. 2014. South China Sea carbonate build-up seismic characteristics.

Katz, D. et al. 2010. Slope Heterogeneity in a Steep-Sided Upper Paleozoic Isolated Carbonate Platform Reservoir, Karachaganak Field, Kazakhstan. In: *SPE Caspian Carbonates Technology Conference*. Society of Petroleum Engineers. Available at: http://www.onepetro.org/doi/10.2118/139960-MS [Accessed: 19 October 2018].

Kendall, C.G.S.C. and Schlager, W. 1981. Carbonates and relative changes in sea level. *Marine Geology* 44(1–2), pp. 181–212. Available at: https://www.sciencedirect.com/science/article/pii/0025322781901183 [Accessed: 7 March 2018].

Kenter, J. et al. 2008. *Facies and Reservoir Quality of the Tengiz Isolated Platform, Pricaspian Basin, Kazakhstan**. Available at: http://www.searchanddiscovery.com/documents/2008/08029kenter/images/kenter.pdf [Accessed: 12 November 2018].

878 Kuznetsov, V.G. 1997. Oil and gas in reef reservoirs in the former USSR. *Petroleum*
879 *Geoscience* 3(1), pp. 65–71. Available at:
880 http://pg.lyellcollection.org/cgi/doi/10.1144/petgeo.3.1.65 [Accessed: 16 May 2018].

881 Larsen, P.-H. 1988. Relay structures in a Lower Permian basement-involved extension
882 system, East Greenland. *Journal of Structural Geology* 10(1), pp. 3–8. Available at:
883 http://www.sciencedirect.com/science/article/pii/0191814188901228?via%3Dihub
884 [Accessed: 9 January 2018].

885 Leeder, M.R. and Gawthorpe, R.L. 1987. Sedimentary models for extensional tilt-
886 block/half-graben basins. *Geological Society, London, Special Publications* 28(1), pp. 139–
887 152. Available at: http://sp.lyellcollection.org/lookup/doi/10.1144/GSL.SP.1987.028.01.11
888 [Accessed: 18 April 2019].

889 Longley, I.M. et al. 2002. The North West Shelf of Australia–a Woodside perspective.
890 *The Sedimentary Basins of Western Australia 3: Proceedings of Petroleum Exploration*
891 *Society of Australia Symposium* , pp. 27–88. doi: 10.1017/CBO9781107415324.004.

892 Marfurt, K.J. and Alves, T.M. 2015. Pitfalls and limitations in seismic attribute
893 interpretation of tectonic features. *Interpretation* 3(1), pp. SB5-SB15. Available at:
894 http://library.seg.org/doi/10.1190/INT-2014-0122.1 [Accessed: 13 December 2017].

895 Marshall, J. et al. 1994. Sahul shoals processes: Neotectonics and Cainozoic
896 environments-cruise 122: Post Cruise Report. *Australian Geological Survey Organisation,*
897 *Canberra* 928, pp. 929–930.

898 Mattos, N.H. et al. 2016. Crestal fault geometries reveal late halokinesis and collapse
899 of the Samson Dome, Northern Norway: Implications for petroleum systems in the Barents
900 Sea. *Tectonophysics* 690, pp. 76–96. Available at:

https://www.sciencedirect.com/science/article/pii/S0040195116301111 [Accessed: 9 October 2018].

Mory, A.J. 1991. *Geology of the offshore Bonaparte Basin, northwestern Australia*. Geological Survey of Western Australia.

Muraoka, H. and Kamata, H. 1983. Displacement distribution along minor fault traces. *Journal of Structural Geology* 5(5), pp. 483–495. Available at: https://ac.els-cdn.com/0191814183900548/1-s2.0-0191814183900548-main.pdf?_tid=2482f564-0056-11e8-96b3-00000aacb360&acdnat=1516723242_6537bfbb2a2794ee099a6e13d001f141 [Accessed: 23 January 2018].

Neuhaus, D. et al. 2004. Quantitative Seismic Reservoir Characterization of an Oligocene Miocene Carbonate Buildup: Malampaya Field, Philippines.

Nordaunet-Olsen, E.M. 2015. Controls on upper Paleozoic carbonate build-up development in the South Central Norwegian Barents Sea. Available at: https://brage.bibsys.no/xmlui/handle/11250/300408 [Accessed: 12 November 2018].

Paumard, V. et al. 2017. Evolution of Late Oligocene - Early Miocene attached and isolated carbonate platforms in a volcanic ridge context (Maldives type), Yadana field, offshore Myanmar. *Marine and Petroleum Geology* 81, pp. 361–387. Available at: https://www.sciencedirect.com/science/article/pii/S026481721630441X?via%3Dihub [Accessed: 7 August 2018].

Pomar, L. 2001. Types of carbonate platforms: a genetic approach. *Basin Research* 13(3), pp. 313–334. Available at: http://doi.wiley.com/10.1046/j.0950-091x.2001.00152.x [Accessed: 23 February 2018].

923 Posamentier, H.W. et al. 2010. Seismic Stratigraphy and Geomorphology of Oligocene
924 to Miocene Carbonate Buildups, Offshore Madura, Indonesia. In: *Cenozoic Carbonate*
925 *Systems of Australasia*. SEPM (Society for Sedimentary Geology), pp. 175–192. Available at:
926 https://pubs.geoscienceworld.org/books/book/1189/chapter/10582235/ [Accessed: 29
927 June 2018].

928 Rankey, E.C. et al. 2019. Seismic architecture of a Miocene isolated carbonate
929 platform and associated off-platform strata (Central Luconia Province, offshore Malaysia).
930 *Marine and Petroleum Geology* 102, pp. 477–495. Available at:
931 https://www.sciencedirect.com/science/article/pii/S0264817219300091 [Accessed: 31
932 January 2019].

933 Rexilius, J.P. et al. 1998a. *Micropalaeontological Analysis Ludmilla-1, Permit AC-P16,*
934 *Bonaparte Basin*. Western Australia.

935 Rexilius, J.P. et al. 1998b. *Micropalaeontological Analysis Mandorah-1, Permit AC-P16,*
936 *Bonaparte Basin*. Western Australia.

937 Rexilius, J.P. and Powell, S.L. 1999a. *Micropalaeontological Analysis Fannie Bay-1,*
938 *Permit AC-P16, Bonaparte Basin*. Western Australia.

939 Rexilius, J.P. and Powell, S.L. 1999b. *Micropalaeontological Analysis Paleogene Section*
940 *Mandorah-1, Permit AC-P16, Bonaparte Basin*. Western Australia.

941 Rosleff-Soerensen, B. et al. 2016. The response of a basin-scale Miocene barrier reef
942 system to long-term, strong subsidence on a passive continental margin, Barcoo Sub-basin,
943 Australian North West Shelf. *Basin Research* 28(1), pp. 103–123. Available at:
944 http://doi.wiley.com/10.1111/bre.12100 [Accessed: 22 August 2018].

945 Ruig, M. de 2000. Seismic Interpretation Report Karmt 3D Survey, Permit AC/P16
946 (Bonaparte Basin, Timor Sea). 16

947 Rusciadelli, G. and Shiner, P. 2018. Isolated Carbonate Platforms of the Mediterranean
948 and their seismic expression – searching for a paradigm. *The Leading Edge* (July). doi:
949 10.1190/tle37070492.1.

950 Saqab, M. and Bourget, J. 2015a. Controls on the distribution and growth of isolated
951 carbonate build-ups in the Timor Sea (NW Australia) during the Quaternary. *Marine and*
952 *Petroleum Geology* 62, pp. 123–143. Available at:
953 https://www.sciencedirect.com/science/article/pii/S0264817215000240 [Accessed: 29
954 January 2018].

955 Saqab, M.M. and Bourget, J. 2015b. Structural style in a young flexure-induced oblique
956 extensional system, north-western Bonaparte Basin, Australia. *Journal of Structural Geology*
957 77, pp. 239–259.

958 Sattler, U. et al. 2009. Drowning history of a Miocene carbonate platform (Zhujiang
959 Formation, South China Sea). *Sedimentary Geology* 219(1–4), pp. 318–331. Available at:
960 https://www.sciencedirect.com/science/article/pii/S0037073809001523 [Accessed: 9 May
961 2019].

962 Schlager, W. 2005. *Carbonate sedimentology and sequence stratigraphy*. SEPM Soc for
963 Sed Geology.

964 Stanton Jr, R.J. 1967. Factors controlling shape and internal facies distribution of
965 organic carbonate buildups. *AAPG Bulletin* 51(12), pp. 2462–2467.

966 Van Tuyl, J. et al. 2018. Pinnacle features at the base of isolated carbonate buildups

marking point sources of fluid offshore Northwest Australia. *GSA Bulletin* . Available at: https://pubs.geoscienceworld.org/gsa/gsabulletin/article/530065/Pinnacle-features-at-the-base-of-isolated [Accessed: 2 May 2018].

Veevers, J.J. 1971. Shallow stratigraphy and structure of the Australian continental margin beneath the Timor Sea. *Marine Geology* 11(4), pp. 209–249. Available at: https://www.sciencedirect.com/science/article/pii/0025322771900260 [Accessed: 15 June 2018].

Walsh, J.J. and Watterson, J. 1991. Geometric and kinematic coherence and scale effects in normal fault systems. *Geological Society, London, Special Publications* 56(1), pp. 193–203. Available at: http://sp.lyellcollection.org/lookup/doi/10.1144/GSL.SP.1991.056.01.13 [Accessed: 29 August 2018].

Whittam, D.B. et al. 1996. MESOZOIC AND CAINOZOIC TECTONOSTRATIGRAPHY OF WESTERN ZOCA AND ADJACENT AREAS. *The APPEA Journal* 36(1), p. 209. Available at: http://www.publish.csiro.au/?paper=AJ95012 [Accessed: 13 February 2018].

Willis, S. 1998. *Ludmilla-1 Well Completion Report, Interpretive Data*.

Willis, S. 1999a. *Fannie Bay-1 Well Completion Report, Interpretive Data*. Available at: http://www.ga.gov.au.

Willis, S. 1999b. *Lameroo-1 Well Completion Report, Interpretive Data*. Available at: http://www.ga.gov.au.

Willis, S. 1999c. *Mandorah-1 Well Completion Report, Interpretive Data*.

Willis, S. 2000. *Mindil-1 Well Completion Report, Interpretive Data*.

Wilson, M.E.. 1999. Prerift and synrift sedimentation during early fault segmentation of a Tertiary carbonate platform, Indonesia. *Marine and Petroleum Geology* 16(8), pp. 825–848. Available at: https://www.sciencedirect.com/science/article/pii/S0264817299000197 [Accessed: 9 May 2019].

Woodall, M. 1990. *Nancar-1/ST Well Completion Report, Interpretive Data*.

Yokoyama, Y. et al. 2001. Sea-level at the Last Glacial Maximum: evidence from northwestern Australia to constrain ice volumes for oxygen isotope stage 2. *Palaeogeography, Palaeoclimatology, Palaeoecology* 165(3–4), pp. 281–297. Available at: https://www.sciencedirect.com/science/article/pii/S0031018200001644 [Accessed: 13 February 2018].

Zampetti, V. et al. 2004. Architecture and growth history of a Miocene carbonate platform from 3D seismic reflection data; Luconia province, offshore Sarawak, Malaysia. *Marine and Petroleum Geology* 21(5), pp. 517–534. Available at: https://www.sciencedirect.com/science/article/pii/S0264817204000315 [Accessed: 13 August 2018].

12 Figure Captions

Figure 1. Bathymetry map showing the study area (seismic survey Karmt 3D) in the Westralian Superbasin (WASB). The study area Karmt 3D is located in the western part of the Sahul Flamingo Nancar Area. Bathymetry data taken from Geoscience Australia. Basin boundaries modified from Longley et al *(2002)*.

Figure 2. Two-way time (TWT) arbitrary seismic profile with NE-SW orientation through the wells Ludmilla-1 and Nancar-1, ST. The main seismic events in the area are

1012 shown: Seafloor (SF), Base Pleistocene (H_6), Base Pliocene (H_5), Base Miocene (H_4), Mid
1013 Eocene (H_3), Top Paleocene (H_2), Base Paleocene (H_1).

1014 Figure 3. 3D perspective visualisation of the interpreted seafloor map from the
1015 Karmt3D seismic volume. The map displays the Karmt Shoals with several isolated
1016 carbonate platforms. (1) Moat channels surrounding ICPs, (2) interior patch reefs, (3)
1017 interplatform channels (4) lagoon, (5) platform rim, (6) platform steep slope.

1018 Figure 4. 3D seismic display showing seismic amplitude corendered with variance
1019 attribute of IL 5333, XL 3335 and time slice -932 ms. Velocity pull-up effects are observed in
1020 section view as fault shadows or fault-like structures (green arrow) and false “uplifted” strata
1021 (red arrow) as a result of vertical changes in velocity. These effects are also seen in time
1022 slices as sub-circular features creating false outlines of the overlying ICPs (green arrows).
1023 Real faults (blue arrows) present continuity in both the time slice and the vertical sections, as
1024 well as the offset in the continuity of the seismic reflectors.

1025 Figure 5. Well log correlation showing the stratigraphic correlation of the area and the
1026 corresponding surfaces interpreted on seismic data. The correlation was performed taking
1027 Ludmilla-1 as the principal well based on gamma-ray (GR) and sonic (DTC) logs as well as
1028 integrated biostratigraphic (foraminiferal and nannoplankton) data taken from raster
1029 composite well logs and micropalaeontological reports (Rexilius et al., 1998b; Rexilius et al.,
1030 1998a; Willis, 1998; Rexilius and Powell, 1999b; Rexilius and Powell, 1999a; Willis, 1999c;
1031 Willis, 1999b; Willis, 1999a). The spatial correlation was carried out by identifying seismic
1032 markers within the wells using seismic data. For well locations and the correlation line see
1033 Figure 9.

1034 Figure 6. Composite log showing GR, RT, NPHI, RHOB and DTC of the Ludmilla-1
1035 well. Integrated biostratigraphic data from sidewall core and cutting samples is presented

1036 with the foraminiferal and nannoplankton zones and their respective ages. Interpreted seismic
1037 markers correspond to seismic horizons. Data taken from Willis (1998).

1038 Figure 7. Cenozoic stratigraphic chart of the northwestern Bonaparte Basin including
1039 seismic stratigraphic units. Modified from Willis (1998) and Saqab and Bourget (2015a). The
1040 seismic section crosses the Ludmilla-1 well for reference.

1041 Figure 8. Isochron maps showing the TWT thickness of the different units. (a)
1042 Isochron of unit 5 from Seafloor horizon to H_6 horizon. (b) Isochron of unit 4 from horizons
1043 H_6 to H_5. (c) Isochron of unit 3 from horizon H_5 to horizon H_4. (d) Isochron of unit 2 from
1044 horizon H_4 to horizon H_3.

1045 Figure 9. Time structure map (a) and coherence map (b) of the base Pleistocene (H_6)
1046 showing the four subdivided zones (separated by green solid lines) of the study area. White
1047 dashed lines represent the interpretation of eight representative faults (F1-F8) with a general
1048 trend of NE-SW. ICP outlines are shown as blue dashed lines. Eight ICPs are identified by
1049 Greek letters (α-θ). The largest relay ramps are mapped, indicated by the light pink polygons.
1050 Small relay ramps are plotted as purple polygons with a red outline. The red line frame
1051 represents the area of interest in which detailed throw measurements have been undertaken to
1052 generate T-Z plots (Fig. 14), T-D plots (Fig. 15) and the high-resolution contour fault throw
1053 map (Fig. 16). The position of the six wells are displayed for reference.

1054 Figure 10. Fault interpretation methodology diagrams. Map view (a) showing a fault
1055 intersection to a time slice. The sections to be taken for fault interpretation and throw
1056 measurement should be perpendicular to the strike at each particular point since the fault is
1057 slightly curved. IL and XL are not useful since they cut the fault at an arbitrary angle β. The
1058 3D view (b) shows a fault with two intersecting sections: one perpendicular to the strike

where the real dip (α_1) can be taken, and a second section intersecting at an arbitrary angle to the strike, which shows the apparent dip of the fault.

Figure 11. Uninterpreted (a) NW-SE seismic line and corresponding interpreted (b) section showing the four different zones in the SW area. Zone 1 presents no faulting. In zone 2, there is a presence of two different fault systems: one in the Neogene-Quaternary and the other one in the Paleogene. An ICP developed above the Neogene-Quaternary faults. Zone 3 presents highly faulted Neogene-Quaternary strata with faults propagating to the surface; as well as Paleogene faulting. Within zone 4, there is only one small fault in the Neogene-Quaternary.

Figure 12. Uninterpreted (a) and corresponding interpreted (b) NW-SE seismic line showing the three different zones in the centre of the study area. Zone 1 in this section shows the presence of normal fault systems throughout the Cenozoic. This zone is characterised by the absence of ICPs. Zone 2 shows the presence of the two fault systems: Neogene-Quaternary and Paleogene. There are faults below the two ICPs in this zone. Zone 3 contains the major fault in the area (fault F1), which propagates to the surface; and minor Neogene-Quaternary normal faults. Zone 4 includes a large fault area with synthetic and antithetic faults.

Figure 13. Uninterpreted (a) and corresponding interpreted (b) NW-SE seismic line showing the three different zones in the NE of the study area. Zone 1 does not present faulting. In zone 2 there is a presence of antithetic faults in the Neogene-Quaternary strata; and there are some synthetic faults in the Cretaceous strata. Zone 3 is highly faulted and the ICP is underlain by the major fault system of fault F1.

Figure 14. Fault throw vertical profiles (T-Z Plot) (black curve) and growth index plots (orange curve) with seismic sections perpendicular to the strike of fault transect F1. Profiles

1083 were taken at various distances, from the southwest tip of the fault transect F1 to the
1084 northeast tip (see distances above each plot). For the location of the lines along the fault
1085 plane, see Figure 15c. Across the area there are two throw maximas (red circles), indicating a
1086 period of fault initiation. The first period of faulting occurred during the Late Paleocene-
1087 Early Eocene with downward fault propagation (dotted arrow line) into unit 1 and upward
1088 fault propagation (solid arrow line) into unit 2. There is a period of fault inactivity between
1089 units 2 and 3 which are represented by an almost constant throw (dashed arrow line). The
1090 second period of faulting occurred during the Late Miocene-Early Pleistocene with a
1091 downward fault propagation into the base of unit 3 (dotted arrow line) and an upward
1092 syndepositional fault propagation into the units 4 and 5 (solid arrow line). The rapid decrease
1093 in throw values near the sea floor reflects the presence of a growth sequence. It can also be
1094 observed as values greater than 1.0 from the growth index plot. Horizontal lines indicate the
1095 interpreted seismic horizons.

1096 Figure 15. Uninterpreted (a) and interpreted (b) view of an area of interest of the
1097 extracted coherence attribute over the H_6 time structure map. Different fault segments
1098 displayed with solid red lines encompass the transect of fault F1. ICP outlines are displayed
1099 in blue. Symbols α, β, γ and δ represent the ICPs crossing the fault F1. The bright yellow
1100 solid line indicates the position of the cross section. (c) Maximum fault throw profile (T-D
1101 Plot) of fault F1 in the Neogene-Quaternary faulting episode shows different interpreted fault
1102 segments with a red line. The blue dashed lines represent the boundaries of the ICPs, and the
1103 green dashed lines indicate the position of the T-Z plots displayed on Figure 14. Relay ramps
1104 are interpreted to be located where two different fault segments intersect and the throw values
1105 are relatively small compared with the maximum throw of both segments. These relay ramp
1106 zones are displayed as pink areas. Uninterpreted (d) and interpreted (e) NW-SE seismic
1107 section shows faults F1a and F1b with the relay ramp structure in between.

Figure 16. High-resolution fault throw surface map along the strike of fault F1 with vertical exaggeration of 3x. Cold colours represent low throw values, whereas warm colours indicate high throw values. The hanging-wall levels of the interpreted horizons (H_1 to H_6) are displayed for reference. The position of the ICPs is drawn with red lines. White line ellipses represent the interpreted individual fault segments. Pink dashed lines represent the large scale fault segments. The areas of low throw values between the individual fault segments are interpreted to be the relay ramps, which are plotted as pink zones. It is clear to see the presence of two faulting events (Paleogene and Neo-Quaternary) mostly divided by the H_4 horizon. The ICP position is interpreted to be related to the presence of relay ramp zones.

Figure 17. Coherence attribute seismic slices of the Karmt3D with a spacing of 64 ms from the base Pleistocene to -216 ms. ICPs are specified with a light blue outline.

Figure 18. Histogram and scatter plots showing (a) histogram with a multimodal area distribution of ICPs; (b) scatter plot of the ICP area against the number of crossing faults; (c) scatter plot of the ICP area versus the number of faults around ICPs within 500 m.

Figure 19. Seismic lines showing the detailed geometry of the different types of ICPs. Horizon H_6 variance map shows the location of the sections (a). The large ICP ε appears to be as type 3 (b) or a combination between type 2 and 3 (c), suggesting that for large platforms the development of ICPs can be a mixture between different types. The ICP η showing the development of the platform as type 2 in the inner relay ramp (d). The ICP γ with a type 2 development with faulted and fractured inner structure (e). Different ICPs developed on a structural high and show an intact internal structure (f and g).

Figure 20. Schematic diagrams showing relay ramp structures and the position of ICPs. (a) ICPs located in the fault tips; (b) development of ICP inside the ramp; (c) relay ramp

formed by several fault segments on a larger scale where ICPs can develop either in fault tips or on the ramp.

Figure 21. Schematic diagram of isolated carbonate platforms as a function of fault throw ratio (T) and carbonate productivity (P). The type 1 ICP develops in structural highs and the ICP is intact. The type 2 ICP develops in an area where there is antecedent faulting, such as on a relay ramp, and where the carbonate productivity is higher than the throw displacement. The type 3 ICP develops initially on a non-faulted zone. Once formed, faults can crosscut the ICP, fracturing their internal structure.

13 Table Captions

Table 1. Seismic character and lithologies of the seismic units interpreted in the study area. Correspondence of the seismic horizons in this work with the horizons in the literature (Willis, 1998).

Epoch	Seismic Unit	Horizon	Comparable horizons	TWT Thickness (ms)	Internal Character, Geometry, and Terminations	Lithology
Pleistocene	5	--Seafloor--	--Sea Bed--	200-650	Moderate- to high- amplitude reflectors. Chaotic under ICBs and parallel to discontinuous in other areas.	Yellowish-grey coarse-grained calcarenites interbedded with silty calcilutites.
Pliocene	4	-- H_6--	-- BPLE --	110-350	Moderate- to high-amplitude continuous reflections. Fault offsets present in the reflectors.	Light olive grey calcareous claystone.
Miocene	3	-- H_5--	-- BPLI --	350-550	Low- to moderate amplitude internal seismic reflections, subparallel to wavy. Highly faulted reflections.	Greenish grey to light grey calcareous claystone interbedded with greenish grey to very light grey argillaceous calcilutites and light grey arenaceous calcarenites.
Oligocene	2	-- H_4--	-- TM3 --	170-550	Low- to moderate amplitude seismic reflections, subparallel to wavy. Seismic reflections intersected by faults.	Light olive-grey calcareous claystone, olive- to yellow-grey argillaceous calcilutites, and yellow-grey to light grey calcilutites with minor yellowish-grey medium to coarse calcarenites.
Late Eocene						
Early Eocene	1	-- H_3--	-- TGREB --	0-120	Moderate- to high- amplitude internal reflections. Unit truncating to the west.	White to light grey very fine to fine grained sandstones.
Paleocene		-- H_2--	-- TE2 --	0-200	Moderate amplitude sub-continuous reflections. Wedge-shaped seismic unit thickening towards the south.	Light olive-grey calcareous claystone and yellow-brown and very light grey medium to coarse grained calcarenites; white to very light calcilutites, interbedded with light grey calcareous claystone.
		-- H_1--	-- T --			

Distribution and growth styles of isolated carbonate platforms as a function of fault propagation

R. Loza Espejel, Tiago .M. Alves, and T. Blenkinsop

3D Seismic Lab, School of Earth and Ocean Sciences, Cardiff University, Main Building-Park Place, CF10 3AT Cardiff, United Kingdom

Highlights:

a) Extensional faults partly control the position and distribution of carbonate platforms off Northwest Australia.

b) Relay ramps can form preferential structures for the initiation and development of isolated carbonate platforms.

c) A relationship among platform growth and fault growth is established.

d) Three models explaining carbonate platform growth are proposed to assess reservoir character.